photonics

MDPI

Article

Photon-Number-Resolving Detection with Highly Efficient InGaAs/InAlAs Single-Photon Avalanche Diode

Yi-Shan Lee [1,*], Tzu-Yang Chen [1], Yu-Ju Chen [1], Wei-Hong Kan [2], Xue-Wen Liu [1] and Jin-Wei Shi [2]

[1] Institute of Photonics Technologies, National Tsing-Hua University, Hsinchu 30013, Taiwan; 109521186@cc.ncu.edu.tw (T.-Y.C.); 110521063@cc.ncu.edu.tw (Y.-J.C.); s111066532@m111.nthu.edu.tw (X.-W.L.)

[2] Department of Electrical Engineering, National Central University, Taoyuan 32001, Taiwan; 110521058@cc.ncu.edu.tw (W.-H.K.); jwshi@ee.ncu.edu.tw (J.-W.S.)

* Correspondence: queenalee@ee.nthu.edu.tw

Abstract: Photon-number-resolving detectors are in high demand for applications in photonic quantum technology. In this study, we demonstrate the photon-number-resolving capabilities of our self-developed, highly efficient InGaAs/InAlAs single-photon avalanche diode. We achieved intrinsic photon number resolving by harnessing the high multiplication gain generated through an avalanche process in the InAlAs multiplication layer. With a maximum single-photon detection efficiency of 46%, we were able to distinguish photon number states up to 5 from the signal probability distribution without encountering avalanche saturation that could otherwise limit the capability of photon number resolving. We reasonably anticipate that the photon-number-resolving accuracy and capability can be further improved once the noise issue in such InGaAs/InAlAs SPADs is carefully managed.

Keywords: single photon avalanche diode; photon number resolving detector; single photon detection efficiency; self-differencing circuit

Citation: Lee, Y.-S.; Chen, T.-Y.; Chen, Y.-J.; Kan, W.-H.; Liu, X.-W.; Shi, J.-W. Photon-Number-Resolving Detection with Highly Efficient InGaAs/InAlAs Single-Photon Avalanche Diode. *Photonics* **2024**, *11*, 724. https://doi.org/10.3390/photonics11080724

Received: 28 June 2024
Revised: 25 July 2024
Accepted: 31 July 2024
Published: 2 August 2024

1. Introduction

Photon-number-resolving (PNR) detection has received growing attention from the academic and professional literature. Due to the capability of discriminating states between different photon numbers, the PNR detector has become indispensable in photonic quantum technology, particularly in quantum computation [1–4], quantum metrology [5–7], and quantum communication [8–10]. In quantum computation, the PNR detector can be used not only for the deterministic preparation of non-Gaussian quantum states but also the implementation of non-Gaussian operations. The performance of a continuous variable quantum-key-distribution (QKD) protocol has been greatly improved in terms of an increased key rate by replacing the standard homodyne receiver with a PNR detector. At the present time, owing to the fact that the PNR detector could not resolve photon numbers faithfully or could provide only a limited capacity for photon numbers, there is still room for improvement in quantum science, such as quantum-state tomography and entanglement-based quantum-state preparation.

In the past few decades, a variety of types of PNR detectors have been developed. The optical field, comprising multiple photons, can be multiplexed into either temporal modes or spatial modes [11–14], enabling the analysis of photon numbers within an optical mode using single-photon detectors. A series array of superconducting single-photon detector (SSPDs), a type of spatial multiplexing scheme, has been demonstrated to achieve PNR, utilizing either an independent readout for each element or a parallel connection with a single output. A similar array arrangement can be applicable to solid-state avalanche diodes, forming multi-pixel photon counters (MPPCs) [13,14]. Such spatially and temporally multiplexed single-photon detectors have been incorporated to measure the photon-number distribution and point values of Wigner functions [11,15–18]. The

number of individual click detectors directly determines the photon-number-resolving capability of these multiplexed single-photon detectors, necessitating a bulky and complex hardware configuration.

An alternative approach, distinct from temporal- or spatial-mode multiplexing, relies on intrinsic energy resolution. The optical transition edge sensor (TES) resolves the number of photons by detecting a slight change in temperature resulting from photon absorption [19]. However, such a device can only be operated at cryogenic temperatures down to the millikelvin scale. To extend the applicability of quantum detection and avoid bulky and expensive cryogenic systems and complex hardware configurations, significant effort has been devoted to developing avalanche diodes with regulating inherent multiplication gain. These detectors, without spatial multiplexing and under conventional operation, can only discriminate zero and nonzero photons. A further implementation such as a self-differencing circuit is required to cancel the gate transient so that the extremely weak current associated with the early onset of avalanche build-up can be discriminated. The first demonstration was reported by [20]. After a decade of effort, the resolvable incident photon number was still limited to 4, or with low distinguishability due to the poor photon detection efficiency under very short gating windows of a few hundred picoseconds and low excess bias [20–23]. The PNR capability of these detectors using single-pixel SPAD, as well as the measurement conditions, has been summarized in Table 1.

Table 1. Comparison of PNR performance across various reports using single-pixel SPAD.

Literature	Gated Frequency (MHz)	Gate Width (ps)	Laser Repetition Rate (MHz)	SPDE (%)	Temp. (K)	Resolvable Photon Number	Figure of Merit, FWHM/ΔV *
2008 InGaAs/InP [20]	622	--	--	10	243	4	0.711
2009 InGaAs/InP [21]	200	500	1	19	233	4	0.69
2010 InGaAs/InP [22]	200	700	1	30.5	243	2	1.11
2019 InGaAs/InP [23]	1000	--	--	40	--	3	1.07
2024 This work	105	1500	26.2	46	200	5	0.99

* In this context, we consistently use Full Width at Half Maximum (FWHM) rather than standard deviation to compare performance. The standard deviation reported in other studies has been converted to FWHM.

InP- and InAlAs-based single-photon avalanche diodes (SPADs) are currently the two primary contenders aimed at near-infrared applications. PNR experiments have been frequently demonstrated by using InP-based SPADs. However, it has been reported that InAlAs-based SPADs can improve performance in terms of breakdown and temperature characteristics [24]. The higher avalanche-breakdown probability in InAlAs potentially results in a higher single-photon-detection efficiency (SPDE) at a lower electric field when compared to InP-based SPADs [25]. Furthermore, the avalanche-breakdown voltage is less sensitive to temperature, providing greater flexibility in adjusting the optimal operating temperature and requiring a less stringent power-supply circuit design. Nonetheless, tunneling generation remains a challenge for InGaAs/InAlAs SPADs, necessitating the engineering of the electric field to mitigate tunneling-induced noise. In this report, we highlight the enhanced capabilities of our self-developed high-efficiency InGaAs/InAlAs

SPAD for PNR applications, leveraging the inherent multiplication gain achieved through an avalanche process. The achievement of high efficiency was made possible through the introduction of the concept of dual multiplication layers, which comprehensively improved the detection performance by reducing the dark count rate, minimizing afterpulses, and enhancing timing jitter [26]. In relation to the enhancements achieved through this innovative structure, we remain committed to the specialized design on the multiplication layer. To effectively showcase the improvement in PNR, we introduce an advanced structure comprising three multiplication layers, featuring a three-staircase electric-field distribution.

2. SPAD Design Concepts

The layer structure and electric-field distribution are shown in Figure 1a,b, respectively. The design concept addresses the trade-off between the dark count rate (DCR) induced by tunneling generation, afterpulsing, and timing jitter. We propose an SPAD structure with a relatively thin multiplication layer compared to conventional SPAD designs, which typically use a multiplication layer at least 1000 nm thick. The detailed layer structure of our SPAD device is illustrated in Figure 1a. The structure was grown by molecular beam epitaxy (MBE) on a semi-insulating InP substrate. We designed a 2000 nm thick absorption layer to enhance photon absorption efficiency. To mitigate carrier accumulation at the abrupt InGaAs/InAlAs heterojunctions, we incorporated two grading layers. The doping concentration of the top field-control layer was carefully selected to maintain a low yet sufficiently high electric-field strength in the absorption layer, enabling effective drift of photogenerated carriers to the multiplication layer. Additionally, by introducing two bottom field-control layers, we segmented the conventional 440 nm thick multiplication layer in a separate absorption, grading, charge, and multiplication (SAGCM) structure with two 100 nm thick top multiplication layers and a 240 nm thick bottom multiplication layer. This segmentation creates a three-stepwise electric-field distribution along the growth direction, as shown in Figure 1b. The electric-field distribution was calculated using Silvaco Technology Computer Aided Design (TCAD) tools.

In our design, the two 100 nm thick top multiplication layers, which do not reach the impact ionization threshold, serve to energize and accelerate carriers towards the bottom multiplication layer. The 240 nm thick bottom multiplication layer then initiates subsequent impact ionizations, resulting in a self-sustaining avalanche process. The top two multiplication layers help build up the initial energy of the carriers and align them uniformly at the starting point, which is instrumental in avoiding the dead-space effect and potentially enhancing the timing jitter. This approach allows us to maintain a suitable applied bias-voltage range while reducing the overall thickness of the multiplication layer.

The dark and illuminated current–voltage characteristics are shown in Figure 1c. The punch-through and breakdown voltages are determined to be 9 V and 55 V, respectively, with the breakdown voltage defined at a dark current of 10 μA. The abrupt rise around 25 V results from the multiple charge layers and depletion regions due to our specialized triple multiplication layer, as illustrated by the layer structure in Figure 1a. Based on the calculated dark current–voltage characteristics and measured capacitance–voltage characteristics curves, the two abrupt rises at approximately 9 V and 25 V likely correspond to the first and second punch-through voltages for the absorption layer and the first multiplication layer.

While demonstrating the improved PNR performance of a single-pixel device, it becomes evident that an array based on such a single-pixel device can indeed achieve an impressive PNR capability. In the following sections, we demonstrate that our self-developed SPAD, utilizing its inherent high multiplication gain provided by introducing a novel structure design, possesses the ability to unambiguously resolve photon numbers up to 5 at a maximum single-photon detection efficiency of 46% without arriving at an avalanche saturation that might impede photon-number-resolving capabilities. Unlike the superconductor-based PNR detector requiring a bulky and expensive cryogenic system, our

device can perform PNR at a temperature very close to room temperature, which facilitates the widespread adoption of PNR detectors.

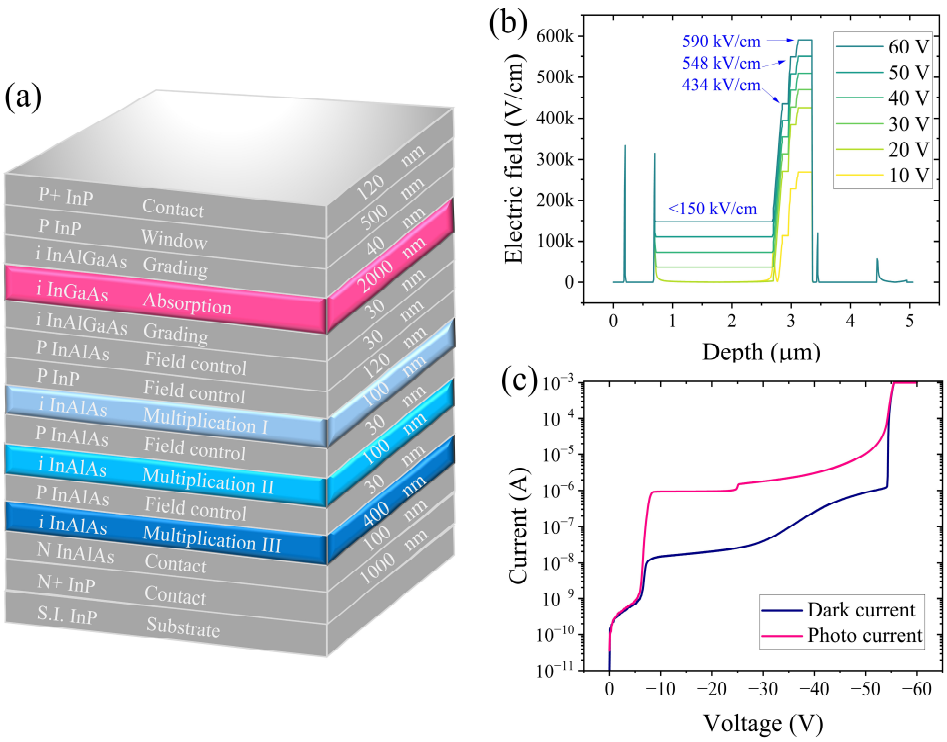

Figure 1. (**a**) Epitaxial layer structure of our self-developed InGaAs/InAlAs SPAD. (**b**) Calculated electric-field distribution along the growth direction. The electric field strengths are as follows for the different layers: 150 kV/cm for the absorption layer, 434 kV/cm for the first multiplication layer, 548 kV/cm for the second multiplication layer, and 590 kV/cm for the third multiplication layer. (**c**) Dark current and photocurrent of our self-developed InGaAs/InAlAs.

3. Experimental Details

The SPADs are operated in gated mode, where the applied voltage bias consists of both a direct current (dc) component and a periodic voltage pulse. The voltage pulse has a frequency of 104.7 MHz and a pulse width of 1.5 ns. The avalanche signal is superimposed onto the capacitive signal coupled through a diode junction. A 1550 nm pulsed laser with a 30 ps pulse duration and a repetition rate of 26.2 MHz, which is one-fourth of the gate frequency, is employed as the photon source. We obtain a faint laser by passing the source through a strong attenuator. To ensure the security of real applications and enable single-photon characterization, the mean photon number in each laser pulse is kept very low. Therefore, the laser beam is attenuated to the average photon number of 0.1 and 1 per laser pulse, respectively, for the purpose of the device characterization and assessment of the PNR capability. In order to resolve the incident photon number, it is crucial to detect the initial current right after the avalanche buildup. To mitigate the capacitive response during the gated-mode operation, we implement a self-differencing (SD) circuit, as depicted in Figure 2a. This SD circuit achieves a suppression ratio of 37.6 dB, effectively eliminating the common capacitive signal and distinguishing the avalanche signal, as shown in Figure 2b,c, respectively. As a result, the minor avalanche signal can be distinguished with a 0.1 mV variation. The measurements are conducted within an LN2 open-cycle cryostat (Optistat CF, Oxford Instruments, Abingdon, UK), capable of cooling the device to 77 K. The electrical signals can be both applied and extracted through the electrical feedthrough of the cryostat. The cooling process effectively suppresses the presence of dark carriers caused by thermal generation. At a temperature of 200 K, the SPAD with a three-staircase electric-field distribution has been tested and shown to exhibit

an SPDE of 46% at a dark count probability (DCP) of 7.5×10^{-3}. The SPDE and DCP dependences on the temperature are shown in Figure 3a. The DCP is recorded over a wide temperature range for various excess biases in Figure 3b. At low excess-bias levels, the effectiveness of cooling in reducing the DCP is limited. This suggests that tunneling generation plays a dominant role in the DCP. It is also worth noting that at a high excess bias, the DCP decreases as the temperature decreases but halts within the temperature range of 200 K to 250 K, indicating the presence of an afterpulsing effect. By balancing the trade-off between afterpulsing effects and thermal generation, we chose to demonstrate the PNR measurement at 200 K. To measure the afterpulsing effect, the output signal is then routed to a time-correlated single-photon counting module (TCSPC) with a timing resolution of 4 ps. The recorded counts are subsequently organized into histograms to determine the afterpulsing probability. The afterpulsing probability increases as the temperature decreases due to the prolonged trap lifetime at lower temperatures. At a temperature of 200 K and an SPDE of 46%, where the PNR is performed, an afterpulsing probability of 21% is observed.

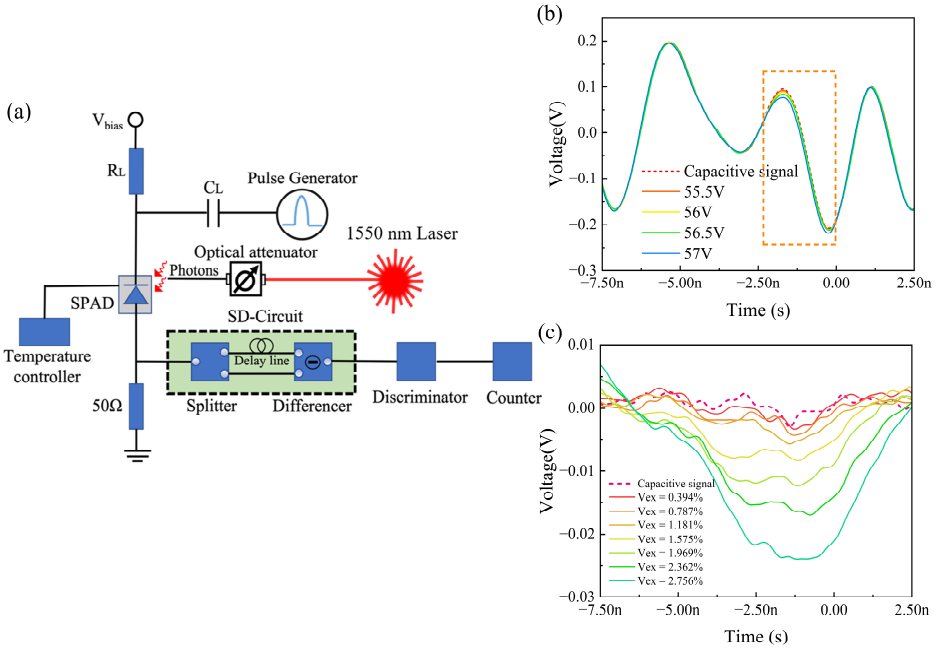

Figure 2. (**a**) Illustration of self-differencing circuit. (**b**) Output signal without self-differencing circuit. (**c**) Avalanche signal obtained after the elimination of the capacitive signal through a self-differencing circuit. The orange dotted region marks the location of the avalanche signal.

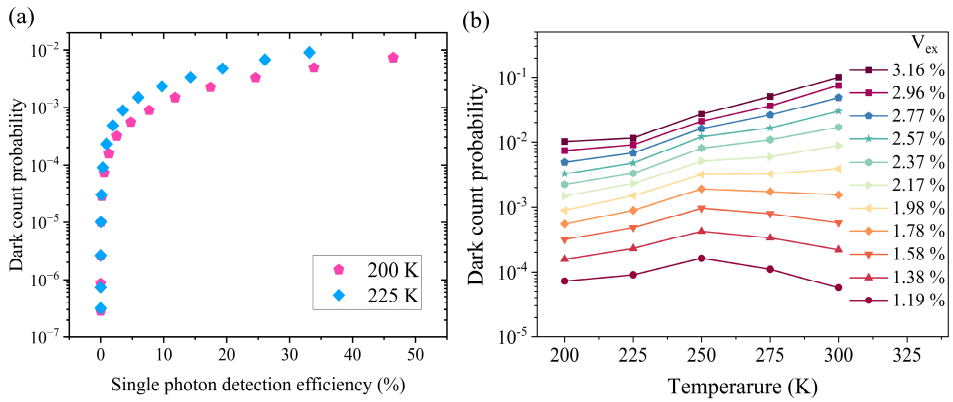

Figure 3. (**a**) DCP as a function of SPDE measured at T = 200 K and 225 K. (**b**) DCP as a function of temperature at different excess-bias levels.

4. Photon-Number-Resolving Performance

An ideal PNR detector delivers an output signal that accurately represents the number of photons of the input signal. However, in practice, non-ideal characteristics of detectors, such as non-unity photon-detection probability and dark noise, limit the maximum number of photons the detector can resolve and affect the certainty of assigning the photon-number state. The photon-number distribution of an attenuated laser would approximately follow a Poisson distribution. By considering both the response function of the detector and the photon-number statistics of the attenuated laser, we can derive the probability of the output signal in response to the input pulse as a combination of each photon-number state, given as:

$$\mathrm{P(V)} = \sum_{n=0}^{\infty} \mathrm{p_n}(\eta) \cdot \rho(\mathrm{n},\ \mathrm{V})\ . \tag{1}$$

where $\mathrm{p_n}(\eta) = \left((\eta\mu_\mathrm{n})^n/n!\right)e^{-\eta\mu_n}$ represents the probability of containing n photon-number state with an average photon number of μ_n, η is the overall detection efficiency of the device, and $\rho(\mathrm{n,V})$ determines the relation function between output signal amplitude and the photon-number state, illustrating the PNR performance in terms of voltage separation (ΔV) and full-width at half-maximum (FWHM). Consequently, the photon-number-resolving performance is recorded by arranging the registered events as a function of avalanche voltage amplitude.

5. Discussion

Figure 4a illustrates the distribution of peak output signal voltages at various SPDEs and at a temperature of 200 K for an average photon number of 1. The observed distribution of peak output signals can be explained using the Poisson superposition of photon-number states as described in Equation (1), taking into account the experimental parameters of the mean photon number and signal amplitude. In Figure 4a, the black line represents the mapping of the 0-photon excited avalanche signal, corresponding to the background noise. The transparent blue line guides the fitted result of the overall photon-number statistics. The other solid lines depict the peak voltage states for different photon-number excited avalanche signals by applying a Gaussian fit to the data. The discrimination level was set to 138 mV to avoid the background noise caused by the small mismatch of the self-differencing circuit, which was independent of the voltage applied on the APD. It is clearly observed from Figure 4b that as the SPDE varies from 24% to 46%, both the signal amplitude of the 1-photon number state and the voltage separation between each photon-number state increase. This is attributed to the higher multiplication gain achieved at a higher excess bias. For all photon-number states up to 5 (n = 5), the signal amplitude consistently exhibits a linear increase with an increasing single-photon detection efficiency (SPDE), implying non-saturated gain even at the maximum SPDE. However, at higher SPDE levels or higher excess bias, our device experiences significant DCR and afterpulsing issues, rendering it unable to detect photons. Furthermore, the spacing between the peaks of each photon-number state is nearly equidistant at the same SPDE. This implies that the amplitude is indeed proportional to the incoming photon number and also suggests a reliable assignment to each photon-number state. The standard deviation, or full width at half maximum (FWHM), of the 1-photon-number state is also plotted as a function of SPDE in Figure 4c. It shows a slight increase with increasing SPDE, suggesting a noise-induced broadening of the photon-number distribution. At the same SPDE, the photon distribution follows the property of Poisson distribution, with the FWHM increasing as the probability of occurrence significantly decreases with an increasing photon-number state. In the literature, the ratio of the standard deviation of the 1-photon-number pulse to the voltage separation is frequently employed as a measure to evaluate the PNR performance. This ratio is subsequently calculated and presented in Table 2, alongside other relevant performance metrics. As the bias voltage increases, the ratio, also named figure of merit (FOM), significantly decreases from 1.361 to 0.99, indicating that PNR capability improves with higher excess-bias voltages. The overlaps between the Gaussian fits to one-photon and two-photon states are further

compared for different SPDE values, as shown in Figure 4d, which is often used to evaluate the performance of PNR detectors. The overlap area significantly decreases as SPDE increases, implying that the discrimination of two neighboring photon-number states is enhanced with higher SPDE. The notably high DCP and afterpulsing observed in the InGaAs/InAlAs SPAD result in a wide FWHM in each photon-number-state distribution and lead to some overlap between them. This is due to the random nature of the DCP and afterpulsing, which hinders the accurate measurement of photon-number statistics. However, the high gain inherent to such a unique structure also offers a certain capacity to identify higher photon-number states. We should further emphasize that, unlike the typically used sub-nanosecond gate widths, our device can resolve photon-number states up to 5 with a substantially larger gate width of 1.5 ns, albeit at the cost of a notable standard error. By shortening the gating pulse duration, the overlap of peaks can be reduced, as this method effectively suppresses both the DCP and the afterpulsing effect.

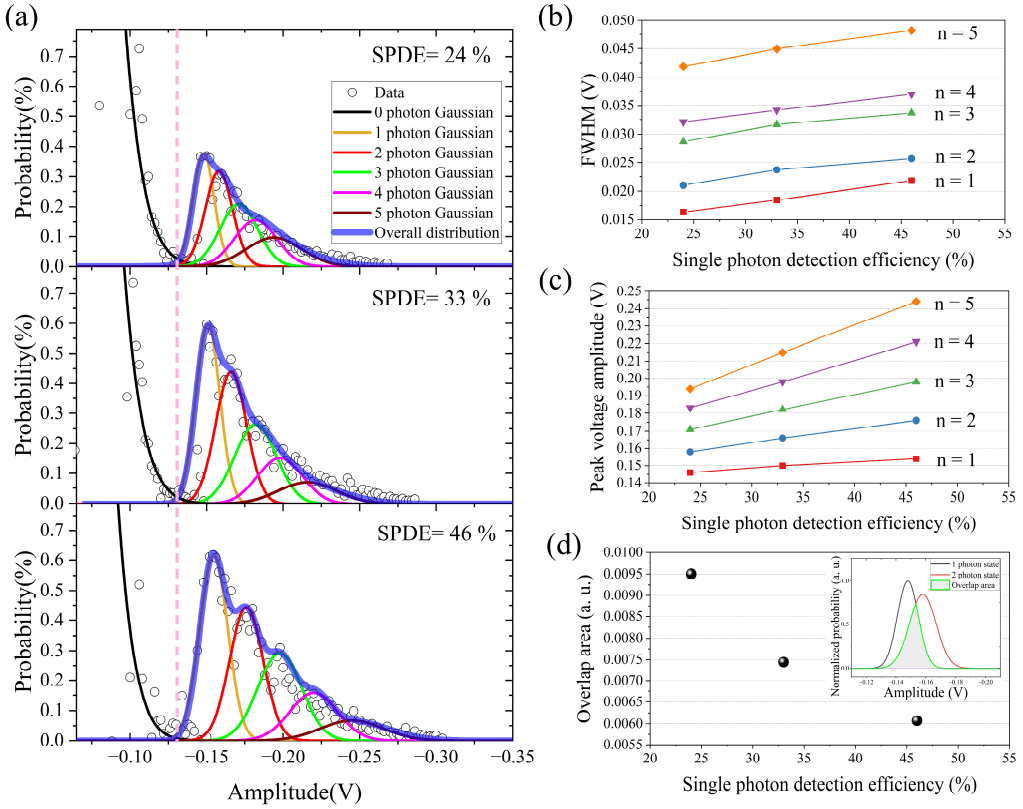

Figure 4. (**a**) Distribution of the peak output signal at different SPDE values of 24%, 33% and 46% at a temperature of 200 K. Each colored line shows the Gaussian fit for different photon-number states. (**b**) Peak voltage amplitude as a function of SPDE for different photon-number states. (**c**) Full width at half maximum as a function of SPDE for different photon-number states. (**d**) Overlap area between the normalized probability distribution of the one-photon and two-photon states. Inset in (**d**): gray region indicates the overlap area.

Table 2. PNR performance at different excess biases.

Excess Bias (%)	SPDE (%)	Separation, ΔV (V)	FWHM (V)	FWHM/ΔV
2.569	24	0.012	0.01634	1.361
2.766	33	0.016	0.01847	1.154
2.964	46	0.022	0.02178	0.99

6. Conclusions

We have demonstrated a photon-number-resolving detector based on a high-efficiency In0.53Ga0.47As/In0.52Al0.48As SPAD. We achieved an SPDE of 46% at 1550 nm, making the detector highly promising for applications in quantum optics and quantum information science, particularly those involving single-photon counting. Notably, this is the first instance of intrinsic photon-number resolving using InGaAs/InAlAs SPAD without multiplexed schemes. We have successfully distinguished photon-number states up to 5, increased the voltage separation, and reduced the overlap area by raising the SPDE, while avoiding avalanche saturation that could limit photon-number-resolving capabilities. The fact that we have not yet reached avalanche saturation implies that there is the potential to further reduce the peak overlap and hence enhance the PNR performance once we successfully address the issue of DCR and afterpulsing in our device. In Table 1, we provide a comparison of PNR performances among recent reports, highlighting the highest resolvable photon-number state we have achieved and demonstrating a comparable photon-number-state distinguishability at a relatively large gate width compared to InP-based SPADs. This work also underscores the potential for higher-efficiency SPADs to enhance the ability to differentiate n from n + 1 photons, a crucial metric for quantum optics applications. By reducing the gating pulse duration, one can further suppress the noise and, consequently, enhance the distinguishability and capability of PNR thanks to the high gain inherent in InAlAs-based SPADs. Alternatively, implementing sinusoidal gating with a filter scheme can better control the gating window and distinguish the avalanche signal from the background noise. The current work has enhanced the PNR performance of a single-pixel SPAD, ensuring its elevated applicability while forming spatial-multiplexed or time-multiplexed photon-number detectors. Unlike a superconductor-based PNR detector requiring a bulky and expensive cryogenic system, our device can perform PNR very close to room temperature, facilitating the widespread adoption of PNR detectors.

Author Contributions: Conceptualization, Y.-S.L. and J.-W.S.; methodology, T.-Y.C.; software, X.-W.L.; validation, T.-Y.C., Y.-J.C. and W.-H.K.; formal analysis, T.-Y.C.; investigation, T.-Y.C.; resources, Y.-S.L.; data curation, Y.-S.L.; writing—original draft preparation, Y.-S.L.; writing—review and editing, Y.-S.L.; visualization, Y.-S.L.; supervision, Y.-S.L.; project administration, Y.-S.L.; funding acquisition, Y.-S.L. All authors have read and agreed to the published version of the manuscript.

Funding: This work was funded by the National Science and Technology Council 112-2221-E-007-109-MY3, 111-2627-M-008-001, 112-2119-M-008-007 and 113-2119-M-008-010.

Institutional Review Board Statement: Not applicable.

Informed Consent Statement: Not applicable.

Data Availability Statement: The data presented in this study are available on request from the corresponding author due to confidentiality agreements.

Conflicts of Interest: The authors declare no conflict of interest.

References

1. Knill, E.; Laflamme, R.; Milburn, G.J. A scheme for efficient quantum computation with linear optics. *Nature* **2001**, *409*, 46–52. [CrossRef]
2. Ralph, T.C.; Gilchrist, A.; Milburn, G.J.; Munro, W.J.; Glancy, S. Quantum computation with optical coherent states. *Phys. Rev. A* **2003**, *68*, 042319. [CrossRef]
3. Kok, P.; Munro, W.J.; Nemoto, K.; Ralph, T.C.; Dowling, J.P.; Milburn, G.J. Linear optical quantum computing with photonic qubits. *Rev. Mod. Phys.* **2007**, *79*, 135–174. [CrossRef]
4. O'Brien, J.L. Optical quantum computing. *Science* **2007**, *318*, 1567–1570. [CrossRef]
5. Matthews, J.C.; Zhou, X.-Q.; Cable, H.; Shadbolt, P.J.; Saunders, D.J.; A Durkin, G.; Pryde, G.J.; O'brien, J.L. Towards practical quantum metrology with photon counting. *NPJ Quantum Inf.* **2016**, *2*, 16023. [CrossRef]
6. Wu, J.-Y.; Toda, N.; Hofmann, H.F. Quantum enhancement of sensitivity achieved by photon-number-resolving detection in the dark port of a two-path interferometer operating at high intensities. *Phys. Rev. A* **2019**, *100*, 013814. [CrossRef]

7. von Helversen, M.; Böhm, J.; Schmidt, M.; Gschrey, M.; Schulze, J.-H.; Strittmatter, A.; Rodt, S.; Beyer, J.; Heindel, T.; Reitzenstein, S. Quantum metrology of solid-state single-photon sources using photon-number-resolving detectors. *New J. Phys.* **2019**, *21*, 035007. [CrossRef]
8. Becerra, F.E.; Fan, J.; Migdall, A. Photon number resolution enables quantum receiver for realistic coherent optical communications. *Nat. Photonics* **2015**, *9*, 48–53. [CrossRef]
9. DiMario, M.T.; Kunz, L.; Banaszek, K.; Becerra, F.E. Optimized communication strategies with binary coherent states over phase noise channels. *NPJ Quantum Inf.* **2019**, *5*, 65. [CrossRef]
10. Afek, I.; Natan, A.; Ambar, O.; Silberberg, Y. Quantum state measurements using multipixel photon detectors. *Phys. Rev. A* **2009**, *79*, 043830. [CrossRef]
11. Laiho, K.; Avenhaus, M.; Cassemiro, K.N.; Silberhorn, C. Direct probing of the wigner function by time multiplexed detection of photon statistics. *New J. Phys.* **2009**, *11*, 043012. [CrossRef]
12. Lita, A.E.; Reddy, D.V.; Verma, V.B.; Mirin, R.P.; Nam, S.W. Development of Superconducting Single-Photon and Photon-Number Resolving Detectors for Quantum Applications. *J. Light. Technol.* **2022**, *40*, 7578–7597. [CrossRef]
13. Lin, J.; Sun, Y.; Wu, W.; Huang, K.; Liang, Y.; Yan, M.; Zeng, H. High-speed photon-number-resolving detection via a GHz-gated SiPM. *Opt. Express* **2022**, *30*, 7501–7510. [CrossRef]
14. Akiba, M.; Inagaki, K.; Tsujino, K. Photon number resolving SiPM detector with 1 GHz count rate. *Opt. Express* **2012**, *20*, 2779–2788. [CrossRef]
15. Laiho, K.; Cassemiro, K.N.; Gross, D.; Silberhorn, C. Probing the negative wigner function of a pulsed single photon point by point. *Phys. Rev. Lett.* **2010**, *105*, 253603. [CrossRef]
16. Bohmann, M.; Tiedau, J.; Bartley, T.; Sperling, J.; Silberhorn, C.; Vogel, W. Incomplete detection of nonclassical phase-space distributions. *Phys. Rev. Lett.* **2018**, *120*, 063607. [CrossRef] [PubMed]
17. Harder, G.; Silberhorn, C.; Rehacek, J.; Hradil, Z.; Motka, L.; Stoklasa, B.; Sánchez-Soto, L.L. Local sampling of the wigner function at telecom wavelength with loss-tolerant detection of photon statistics. *Phys. Rev. Lett.* **2016**, *116*, 133601. [CrossRef]
18. Ding, C.J.; Rong, Y.Y.; Chen, Y.; Chen, X.L.; Wu, E. Direct Measurement of Non-Classical Photon Statistics with a Multi-Pixel Photon Counter. *J. Electron. Sci. Technol.* **2019**, *17*, 204–212. [CrossRef]
19. Hattori, K.; Konno, T.; Miura, Y.; Takasu, S.; Fukuda, D. An optical transition-edge sensor with high energy resolution. *Supercond. Sci. Technol.* **2022**, *35*, 095002. [CrossRef]
20. Kardynał, B.E.; Yuan, Z.L.; Shields, A.J. An avalanche-photodiode-based photon-number-resolving detector. *Nat. Photon.* **2008**, *2*, 425–428. [CrossRef]
21. Chen, X.; Wu, E.; Xu, L.; Liang, Y.; Wu, G.; Zeng, H. Photon-number-resolving performance of the InGaAs/InP avalanche photodiode with short gates. *Appl. Phys. Lett.* **2009**, *95*, 131118. [CrossRef]
22. Chen, X.; Wu, E.; Wu, G.; Zeng, H. Low-noise high-speed InGaAs/InP-based single-photon detector. *Opt. Express* **2010**, *18*, 7010–7018. [CrossRef] [PubMed]
23. Liang, Y.; Liu, Z.; Fei, Q.; Zeng, H. GHz Photon-number-resolving Detection with InGaAs/InP APD. In *CLEO: Applications and Technology*; Optica Publishing Group: Bellingham, WA, USA, 2019; p. JTu2A-40. [CrossRef]
24. Cao, S.; Zhao, Y.; Feng, S.; Zuo, Y.; Zhang, L.; Cheng, B.; Li, C. Theoretical Analysis of InGaAs/InAlAs Single-Photon Avalanche Photodiodes. *Nanoscale Res. Lett.* **2019**, *14*, 3. [CrossRef] [PubMed]
25. Mun, S.C.L.T.; Tan, C.H.; Dimler, S.J.; Tan, L.J.J.; Ng, J.S.; Goh, Y.L.; David, J.P.R. A Theoretical Comparison of the Breakdown Behavior of In0.52Al0.48As and InP Near-Infrared Single-Photon Avalanche Photodiodes. *IEEE J. Quantum Electron.* **2009**, *45*, 566–571. [CrossRef]
26. Lee, Y.-S.; Liao, Y.-M.; Wu, P.-L.; Chen, C.-E.; Teng, Y.-J.; Hung, Y.-Y.; Shi, J.-W. In0.52Al0.48As Based Single Photon Avalanche Diodes with Stepped E-Field in Multiplication Layers and High Efficiency Beyond 60%. *IEEE J. Sel. Top. Quantum Electron.* **2021**, *28*, 3802107. [CrossRef]